Chemical Engineering Science 199 (2019) 388–397

Contents lists available at ScienceDirect

Chemical Engineering Science

journal homepage: www.elsevier.com/locate/ces

Development of wide bandgap perovskites for next-generation low-cost CdTe tandem solar cells

Timothy D. Siegler [a], Tushar M. Shimpi [b], Walajabad S. Sampath [b], Brian A. Korgel [a,*]

[a] McKetta Department of Chemical Engineering and Texas Materials Institute, The University of Texas at Austin, Austin, TX 78712-1062, USA
[b] Next Generation PV Center, Department of Mechanical Engineering, Colorado State University, Ft. Collins, CO 80523, USA

HIGHLIGHTS

- The bandgap of methylammonium bromide is suited for perovskite-CdTe tandems.
- Low optical transmittance or haze in the perovskite layer will limit the tandem potential.
- Haze in the perovskite layer results from film nonuniformity or wrinkling.
- Reducing haze in wide bandgap perovskites is needed for efficient tandem cells.

GRAPHICAL ABSTRACT

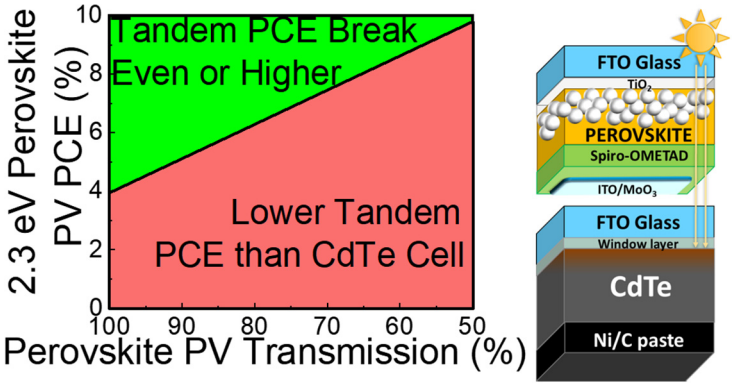

ARTICLE INFO

Article history:
Received 21 October 2018
Received in revised form 6 January 2019
Accepted 12 January 2019
Available online 24 January 2019

Keywords:
Perovskites
Cadmium telluride
Tandem solar cell
Optical haze
Photovoltaics

ABSTRACT

To continue towards long-term reduction in the price of energy generated by photovoltaic (PV) solar cells, technological innovations are needed to achieve significant increases in device efficiency without increasing manufacturing costs. One approach is to utilize the existing capability to manufacture thin film CdTe PVs at very low cost and add another inexpensive thin film absorber to create a tandem solar cell to improve device efficiency. For this, a semiconductor with an optimal bandgap must be identified, along with a suitable device architecture. The wide bandgap perovskite methylammonium lead bromide ($CH_3NH_3PbBr_3$, MAPBr) has a well-matched band gap of 2.3 eV for a CdTe tandem device. It can be processed at relatively low temperature, and is also suitable for CIGS and all-perovskite tandems. We fabricated MAPBr PVs and found that optical scattering, or haze, was significant in these perovskite layers. This limits the transmitted light reaching the bottom cell. The performance of a four-terminal (4T) perovskite-CdTe tandem cell was modeled using the 1D Solar Cell Capacitance Simulator (SCAPS) software package to determine how much haze could be tolerated and still achieve an efficiency boost compared to the CdTe cell.

1. Introduction

A photovoltaic (PV) solar cell is a solid-state semiconductor device that converts sunlight directly to electricity and does not generate any pollution, emissions or greenhouse gases during operation (Nelson, 2003). PV devices represent an important

* Corresponding author.
E-mail addresses: tsiegler@utexas.edu (T.D. Siegler), sampath@engr.colostate.edu (W.S. Sampath), korgel@che.utexas.edu (B.A. Korgel).

https://doi.org/10.1016/j.ces.2019.01.003
0009-2509/

renewable energy resource that is helping to address the global challenge of energy sustainability. One of the biggest successes in the PV industry in recent years is that utility-scale PV has achieved cost-competitiveness with fossil fuels without subsidy in certain situations (<US$ 0.04–0.05/kWh) (Lazard, 2018). This has driven significant demand for solar; for example, the US installed a record 14.7 GW in 2016, nearly double the installed capacity of 2015 (SEIA, 2017). In 2016, the PV market broke several volume records with continued global expansion, bringing the market to at least 75 GW (IEA, 2017). Nonetheless, even with 50% year to year growth in the PV market in 2016, only 1.8% of the world's electricity generation is from solar. In the US—the second largest market in the world behind China—PV still contributes only about 1.3% of total electricity generation (IEA, 2017). Even so, solar adoption is expected to continue to rise significantly and it is anticipated that by 2040, 35% of all new electricity generation capacity will be from solar (Henbest, 2015). Increased solar adoption will continue to require technology improvements, but many believe that these can be accomplished in the near-term by incremental improvements in silicon and CdTe solar cell manufacturing (Green, 2018). However, in the longer term, more significant technology improvements must be made to maintain the ongoing trend in solar cell cost reductions and increased adoption. It has been suggested that solar cells with 30% efficiency made with manufacturing costs that are similar to or lower than those for silicon or CdTe panels will be needed by 2040 to maintain the current cost expectations (Mayer, 2015). These efficiencies exceed the theoretical efficiencies of single junction silicon or CdTe solar cells and the only way to reach these efficiencies is through the development of tandem or multijunction solar cells that combine multiple light absorbers with different bandgap energy (Todorov et al., 2018; Werner et al., 2018a; Green, 2018). There are already commercially available multijunction solar cells, but these are either much too expensive, as in the case of III–V multijunction devices (Dimroth, 2006) used only in space applications or concentrated solar cell schemes, or too inefficient for widespread power production, as in the case of thin film a-Si:H devices (Shah et al., 1999) found in consumer electronics applications. Therefore, there has been an active search to develop a next-generation, low-cost thin film tandem solar cell technology that can yield the high efficiencies needed to continue long-term price reductions of solar power.

At the moment, the most commercially successful thin film solar cell technology is CdTe. Although Si dominates the solar cell market, CdTe PVs are less expensive to fabricate and—especially because of recent improvements in efficiency—CdTe has consistently demonstrated the lowest cost for utility-scale power production (Munshi and Sampath, 2016; Munshi et al., 2018). CdTe solar cells are advantageous due to their low energy manufacturing and payback time compared to silicon and CIGS technology (Alsema and de Wild-Scholten, 2006; Raugei et al., 2007). For this reason, tandem solar cells based on CdTe have been widely discussed in the literature, predominantly in conjunction with either silicon or copper indium gallium selenide (CIGS) (Todorov et al., 2018; Sofia et al., 2018). However, the bandgap of CdTe of 1.5 eV is not optimally suited for tandem cell operation with either of these materials.

Other semiconductor materials have been proposed for tandem devices with CdTe, such as wide bandgap CdMgTe, CdZnTe (Swanson et al., 2018), or lower bandgap HgCdTe (Compaan et al., 2004), but the high processing temperatures of these materials can damage underlying CdTe layers or be damaged by the CdTe deposition process when paired in a tandem configuration (Compaan et al., 2004). Perovskites, because of their lower processing temperature and high efficiencies, offers an interesting possibility for a thin film tandem cell configuration with CdTe. For instance, solar cells based on hybrid organic-inorganic perovskites (HOIPs) have achieved power conversion efficiencies in excess of 23% (www.nrel.gov/pv/assets/images/efficiency-chart-20180716.jpg). It has been this high efficiency, along with the low temperature processing and band gap tunability of HOIP thin films, that have made HOIPs attractive candidates for tandem PVs with a variety of different materials (Green et al., 2014; Lal et al., 2017; Liu et al., 2013). Tandem PVs have been made with HOIPs coupled to silicon (Adhyaksa et al., 2017; Albrecht et al., 2016b, 2016a; Ba et al., 2018; Bailie et al., 2015; Bett et al., 2017; Bush et al., 2017, 2016; Chen et al., 2016; Duong et al., 2017, 2016; Fan et al., 2017; Hanne Degans, 2017; Jaysankar et al., 2018, 2017; Jošt et al., 2016; Li et al., 2017; Löper et al., 2015; Mailoa et al., 2015; McMeekin et al., 2016; Peng et al., 2017; Ramírez Quiroz et al., 2018; Sahli et al., 2018a, 2018b; Schneider et al., 2014; Shi et al., 2015; Song et al., 2016; Uzu et al., 2015; Werner et al., 2018b, 2018a, 2016a, 2016c, 2016b, 2015; Wu et al., 2017; Yaokang Zhang et al., 2018; Zheng et al., 2018), CIGS (Bailie et al., 2015; Fu et al., 2016, 2015; Guchhait et al., 2017; Han et al., 2018; Jang et al., 2017; Kranz et al., 2015, 2013; Paetzold et al., 2017; Pisoni et al., 2017; Shen et al., 2018; Todorov et al., 2015; Uhl et al., 2017; Yang et al., 2015), CZTS (Todorov et al., 2014), organic (Chen et al., 2018), polymer (Chen et al., 2015; Liu et al., 2016), DSSC (Kinoshita et al., 2015), quantum dot (Karani et al., 2018; Kim et al., 2018a), and other HOIP PVs (Eperon et al., 2016; Forgács et al., 2017; Heo and Im, 2016; Jiang et al., 2016; Leijtens et al., 2018; Rajagopal et al., 2017, p. 201; Sheng et al., 2017, 2015; Yang et al., 2016; Zhao et al., 2018, 2017). Perhaps surprisingly, there has been little discussion about coupling HOIPs in tandem with CdTe PV technology, in spite of verified 22% PCE CdTe devices (Green et al., 2018) and commercial success of CdTe module manufacturers. Furthermore, with an effective top absorber layer, CdTe is theoretically predicted to make efficient triple junction solar cells when coupled with silicon or germanium (Vos, 1980). Finally, CdTe-HOIP tandems offer the potential for low cost manufacturing. For example, a recent technoeconomic study (Sofia et al., 2018) showed that CdTe-CIGS tandems could achieve levelized cost of electricity (LCOE) as low as US$ 0.095/kWhr for residential solar and US$ 0.04/kWh for utility scale solar, and HOIP-CdTe tandems could prove to be even cheaper, as other studies have shown that perovskite PVs are likely to be less expensive than CIGS (Song et al., 2017).

Here, we address the challenges that may be hindering the development of perovskite-CdTe tandem PVs and outline the prospects for this architecture going forward. We fabricate PVs from wide bandgap $CH_3NH_3PbBr_3$ (MAPBr) and demonstrate that these materials can provide reasonable efficiency as a top absorber layer, but that they also have high optical haze, which limits the light absorption by the CdTe layer and the performance of the perovskite-CdTe tandem cell. We use the Solar Cell Capacitance Simulator (SCAPS) software package to simulate a four-terminal (4T) tandem MAPBr-CdTe architecture to determine how much haze could be tolerated in the perovskite layer in such a device to still achieve an enhancement in device efficiency over the single-junction CdTe cell.

2. Materials and methods

2.1. Materials

Dimethylformamide (99.8% anhydrous), dimethylsulfoxide (≥99.9% anhydrous), zinc purum powder (99%), titanium diisopropoxide bis-acetylacetonate (75% in isopropanol), 1-butanol (99.8% anhydrous), titanium tetrachloride (99.9%), chlorobenzene (99.8% anhydrous), lithium bistrifluoromethanesulfonimidate (99.95%), acetonitrile (99.8% anhydrous), and 4-*tert*-butylpyridine

(96%) were purchased from Sigma-Aldrich. Ethanol (200 proof, ≥99.5%) and reagent-grade hydrochloric acid (37%) were purchased from Fisher Chemical. Lead bromide ($PbBr_2$) was purchased from Alfa Aesar (Ultradry, 99.999% #AA350703-06). Methylammonium bromide (CH_3NH_3Br, MABr) and 30 NR-D Nanoparticulate Titanium Dioxide paste were purchased from Greatcell Solar. Spiro-OMeTAD (N^2,N^2,$N^{2'}$,$N^{2'}$,N^7,N^7,$N^{7'}$,$N^{7'}$-octakis(4-methoxyphenyl)-9,9′-spirobi[9H-fluorene]-2,2′,7,7′-tetramine) was purchased from Merck. Tin-doped indium oxide (ITO) sputter targets were purchased from Kurt J. Lesker (99.99% In_2O_3:SnO_2 9:1), and glass coated with fluorene-doped tin oxide (FTO) was purchased from Hartford Glass Co.

2.2. Fabrication and processing

2.2.1. TiO_2 substrate preparation

FTO substrates (2.5 cm × 2.5 cm) were cleaned with commercial dish soap (Dawn), doubly-distilled deionized water (DI-H_2O), and ethanol and a 0.8 cm × 2.5 cm area of FTO was etched away from the side of the substrate using concentrated HCl and zinc powder. The etched FTO glass was thoroughly washed in DI-H_2O and ethanol, immediately followed by 30 min of bath sonication in ethanol. Following sonication and one hour of UV-ozone exposure (Jelight Company Incorporated Model 42 UVO Cleaner), the n-type TiO_2 contact layers were cast onto the glass substrates. Following the methods of Christians et al. (2015), 75 wt% titanium diisopropoxide bis-acetylacetonate in isopropanol (TAA) was diluted to 72.5 μL/mL in anhydrous 1-butanol, while 210 g of 30 NR-D nanoparticle TiO_2 paste was mixed 3 mL of ethanol, forming a 70 mg/mL paste solution. The TAA solution was spin-coated at 700 rpm for 10 s, followed by 1000 rpm for 10 s and 2000 rpm for 30 s, and then heated for 10 min at 125 °C. Then the TiO_2 paste suspension was spin-coated onto the substrate using the same procedure as used for the TAA solution and heated for 5 min at 70 °C. Finally, the TiO_2 films were annealed for 1 h in air at 550 °C, which yields a film of 30 nm of compact TiO_2 under 150 nm of mesoporous TiO_2. The substrates were immersed for 10 min in 20 mM aqueous $TiCl_4$ at 90 °C and then heated in air at 500 °C for 30 min.

2.2.2. $CH_3NH_3PbBr_3$ (MAPBr) deposition

Methylammonium lead bromide ((CH_3NH_3)$PbBr_3$; MAPBr) films were deposited in a nitrogen glove box (<5 ppm O_2, H_2O) following published procedures (Jesper Jacobsson et al., 2016). In a vial, 459 mg of $PbBr_2$ and 124 mg of CH_3NH_3Br were dissolved in 0.8 mL of DMF and 0.2 mL of DMSO for 2 h at room temperature, yielding a solution of 1.25 M $PbBr_2$ and 1.11 M CH_3NH_3Br in 4:1 v/v DMF:DMSO. Then, 50 μL of the solution was dropped onto the 6.5 cm^2 TiO_2-coated substrate as a thin layer and then spun at 1000 rpm for 10 s followed by 4000 rpm at 30 s. After 15 s of the second spin coating step, 100 μL of anhydrous chlorobenzene was dropped onto the center of the substrate. The substrates were heated in the glove box for 1 h at 100 °C.

2.2.3. Solar cell fabrication

Photovoltaic devices (PVs) were fabricated by spin coating spiro-OMeTAD onto the MAPBr films. Spiro-OMeTAD was dissolved in 72 mg/mL anhydrous chlorobenzene, along with 7.5 μL/mL 4-*tert*-butylpyridine and 24 μL/mL lithium bistrifluoromethanesulfonimidate (LiTFSI) solution (170 mg LiTFSI salt in 1 mL acetonitrile). The spiro-OMeTAD solution was spin-coated onto the MAPBr film at 5000 rpm for 30 s. The substrate was placed in a desiccator for >12 h and then 100 nm of indium-doped tin oxide (ITO) was deposited by *rf* sputtering (Voggu et al., 2017).

2.3. Materials characterization

UV–Vis-NIR absorbance and absorptance spectroscopy was performed using an Aligent Cary 5000 UV–Vis-NIR spectrophotometer with a PbS near infrared (NIR) detector and a photomultiplier tube. Absorptance measurements were collected in an Aligent Diffuse Reflectance Accessory DRA-2500 (DRA) using a center mount holder attachment with the direct beam aimed at ∼8° relative to the angle of incident light. For reflectance and diffuse reflectance measurements, samples were mounted on the black cover of a Labsphere URS-99-020 reflectance standard in the reflectance port of the DRA with a PbS NIR detector and photomultiplier tube. Diffuse reflectance was collected with the light trap that came standard with the DRA-2500 positioned at ∼10° relative to the incident beam with the direct reflectance beam aimed at the trap (Holmberg et al., 2012).

Differential Image Contrast (DIC) images were acquired using a Leica DM2500 Compound Light Microscope with polarized plates positioned between the source and sample, and between the sample and camera.

Scanning electron microscopy (SEM) images were acquired with a Hitachi S-5500 SEM/STEM using an accelerating voltage of 30 kV and an emission current of ∼15 μA in SEM mode. For SEM imaging, MAPBr films were prepared following the procedures used to fabricate PVs, except that the substrates were cut pieces of a p-type Si wafer with a resistivity of 10 Ω cm. The Si wafer was exposed to UV-ozone for 1 h before MAPBr deposition. The substrate was electrically grounded to the SEM mount with carbon tape prior to imaging.

PV device performance was measured using a xenon lamp and a Keithley 2400 general purpose source meter. Current-voltage (*J-V*) curves were measured using a constant voltage sweep rate of 150 mV/s. There was no voltage or light biasing before taking the measurements, or between forward and reverse sweeps. Incident light was passed through an AM 1.5 filter and set at one sun intensity (100 mW/cm^2) via calibration with a Hamamatsu single crystal silicon diode.

2.4. SCAPS device simulations

The device response of CdTe PVs was simulated using the SCAPS software package (Burgelman et al., 2000; Kephart et al., 2015). Tables S1 and S1–S3 list the parameters used for the calculations. Fig. S1 shows the PV architectures that were simulated. In modeling CdTe devices with 15.5% power conversion efficiency (PCE), two types of defect states were included: a CdS/CdTe interfacial defect with 10^{10} cm^{-2} density ($S_n = 10^5$) and a bulk CdTe defect with 10^{14} cm^{-2} density (Kephart et al., 2015). The work function of the back contact was taken to be 5.4 eV. CdTe devices with 22.05% PCE were simulated by removing these defects and increasing the work function of the back contact to 5.6 eV.

In modeling CIGS devices, two types of defects similar to those used for the 15.5% PCE CdTe devices were included. The parameters for the CIGS device simulations were taken from the "Numos CIGS baseline.def" file that accompanies the SCAPS software (Chelvanathan et al., 2010). Table S1 lists the material properties and defect densities used in the simulations.

For all-perovskite tandem devices, the MAPI device layer was simulated using the MAPI model found in SCAPS 3.307 titled "Realistic perfect MAPI cell.def." These parameters are provided in Table S2. The modeling of amorphous silicon (a-Si) cells was done following the procedures of Lee et al. (2009) with the defect concentrations shown in Table S3. Table S3 also shows the other bulk material parameters used in the model calculations.

The device response of the bottom cell in four-terminal (4T) solar cells were simulated by filtering the light incident on the

bottom cell. The total device response of the 4T device was then calculated based on the combined device responses of the top and bottom cells in the 4T tandem configuration.

3. Results and discussion

By combining a CdTe PV with another absorber layer in a tandem configuration, the solar cell can achieve higher device efficiency by exploiting a wider range of the solar spectrum and reducing thermalization losses (Todorov et al., 2018; Werner et al., 2018a; Green, 2018; Yang et al., 2018; Yu et al., 2018). The first consideration of designing a perovskite-CdTe tandem cell is to determine the optimal band gap of the perovskite. Once this is known, a suitable material needs to be identified. And finally, an architecture that will accommodate the materials and the processing constraints must be realized (Nelson, 2003).

3.1. Materials property considerations for a HOIP-CdTe tandem cell

Zincblende CdTe has a band gap of 1.5 eV (Kephart et al., 2015; Munshi et al., 2018). Recent high efficiency CdTe devices have employed a selenium grading that lowers the band gap to 1.42 eV (Munshi et al., 2018), and therefore, the optimal CdTe tandem cell with 1.42 eV CdSeTe requires either a bottom cell absorber layer with a band gap of 0.85 eV (Mailoa et al., 2016; Vos, 1980) or a top cell with a wider band gap of 2.0–2.3 eV (Rühle, 2017). In terms of low bandgap perovskites as a bottom layer, $MAPb_{0.5}Sn_{0.5}PbI_3$ offers the lowest band gap yet observed from an HOIP (at 1 atm pressure), which is 1.17 eV (Hao et al., 2014b). While this is slightly higher than desired, it is not too far from the optimal band gap value (Mailoa et al., 2016; Vos, 1980). However, tin-containing HOIPs—including $MAPb_{0.5}Sn_{0.5}PbI_3$—undergo rapid oxidative degradation in air (Hao et al., 2014b, 2014a) and have not performed well in solar cells (Kapil et al., 2018). Another alternative could be the HOIP-inspired double perovskite, $Cs_2AgTlBr_6$, which has recently been reported with a band gap of 0.95 eV, but solar cells of this material have not yet been fabricated (Slavney et al., 2018). Using a wider bandgap HOIP as a top cell for a perovskite-CdTe tandem cell offers more options.

Fig. 1a provides a summary of the band gap energy of HOIP materials that might be used in a perovskite-CdTe tandem cell architecture. The HOIPs that have exhibited very high PV device efficiency like MAPI, FAPI and $CsPbI_3$ have band gaps that are too similar to CdTe and CdSeTe for tandem cells (Mailoa et al., 2016; Rühle, 2017; Vos, 1980). By incorporating bromide into these materials, the band gap can be increased above 2 eV as needed for tandem cells with CdTe (Kulbak et al., 2016; Noh et al., 2013); however, most HOIP alloys with band gap energies in the range between 1.8 and 2.2 eV have been found to be unstable, exhibiting spontaneous photoinduced phase segregation (Hoke et al., 2015; Rehman et al., 2015). This leaves the bromide HOIPs such as $FAPbBr_3$ (E_g = 2.26 eV), $MAPbBr_3$ (E_g = 2.3 eV), and $CsPbBr_3$ (E_g = 2.35 eV) as the most promising candidate materials for HOIP-CdTe tandems.

3.2. Architecture design considerations of a HOIP-CdTe tandem cell

The tandem cell can be configured into either a mechanically stacked four-terminal (4T) design or a monolithically integrated two-terminal design (2T). There is a preference in industry towards monolithic 2T devices, due to their lower operational complexity and balance of system (BoS) costs (Sofia et al., 2018; Yu et al., 2018). Monolithic 2T perovskite tandem cells have been made on Si (Yang et al., 2018), CIGS (Guchhait et al., 2017) and other perovskites (Eperon et al., 2016) to achieve enhanced efficiency. For

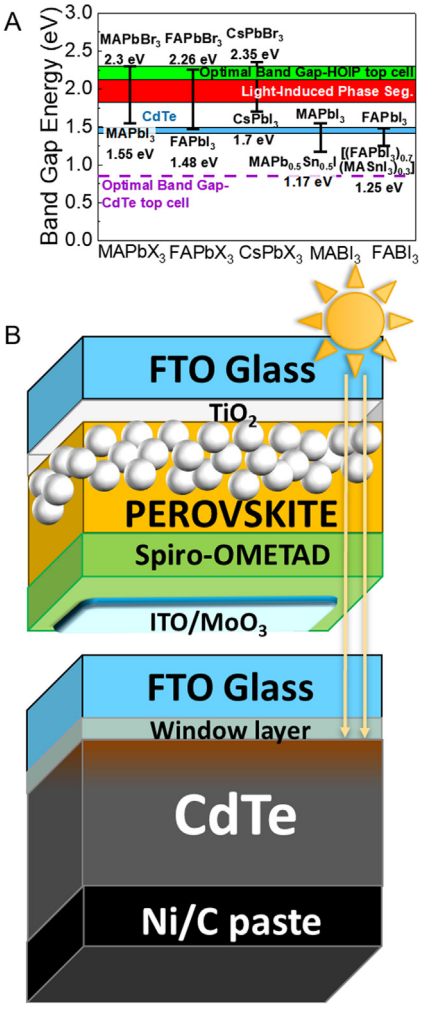

Fig. 1. (A) Summary of the band gap energies of known perovskite materials compared to the band gap range of CdSeTe used in CdTe PV devices (1.42–1.5 eV). The band gap energies are taken from (Eperon et al., 2015; Hao et al., 2014b; Kulbak et al., 2016; Lee et al., 2014; Noh et al., 2013; Parrott et al., 2018; Rehman et al., 2015; Sutton et al., 2016; Todorov et al., 2014; Uzu et al., 2015; Wang et al., 2018). Most HOIPs with bandgap energies between 1.8 and 2.2 eV undergo light-induced phase segregation that limits device performance (Hoke et al., 2015; Rehman et al., 2017, 2015). (B) Proposed 4T architecture of a HOIP-CdTe tandem PV. The high thermal processing temperature of the CdTe layer, the poor device performance of superstrate CdTe devices with reverse illumination, and the low efficiency of CdTe PVs with a substrate configuration limits the potential for monolithic two-terminal (2T) HOIP-CdTe tandem designs.

perovskite-CdTe tandems, 2T device integration will be a challenge because of the way high efficiency CdTe PVs are fabricated.

CdTe PVs are superstrate devices that have an n-type window layer of CdS (or more recently, a buffer layer of MgZnO (Kephart et al., 2016)) that is first deposited on FTO-coated glass, followed by the CdTe absorber layer. The CdTe thin films are vacuum deposited at a substrate temperature of 550 °C and then treated with $CdCl_2$ at 450 °C to achieve commercially suitable device efficiency (Kephart et al., 2015; Munshi et al., 2018). In a 2T HOIP-CdTe tandem, one would optimally design the structure to have the HOIP layer positioned between the glass and the CdTe absorber. This is not possible because the CdTe would need to be deposited onto the HOIP-on-glass layer and the CdTe deposition temperature is considerably higher than the typical decomposition temperature of most HOIP PVs of about 200 °C (Alberti et al., 2017; Domanski et al., 2016; Long et al., 2018). A monolithic HOIP-CdTe tandem solar cell would therefore require deposition of the HOIP layer onto

the CdTe device layer. This would require significant changes in the design of the CdTe device. If the perovskite were simply deposited on the CdTe layer, the device would require illumination on the side opposite to the window layer of the CdTe device. CdTe PVs are well-known to require illumination from the window layer for proper operation (Brown and Wu, 2009; Durose et al., 1999). In fact, this requirement has long inhibited the short wavelength spectral response of CdTe devices (Durose et al., 1999; Kephart et al., 2015). Therefore, this configuration also seems untenable. The final monolithic option would be to employ an inverse CdTe device in a substrate configuration (i.e., CdTe deposited on the FTO-coated glass followed by the window layer of CdS or MZO) and then deposit the perovskite device layer in a p-i-n architecture. This strategy introduces efficiency issues, as inverse substrate CdTe devices have yet to achieve a PCE above a relatively modest 14% (Kranz et al., 2013). Therefore, in order to create an efficient 2T monolithic HOIP-CdTe tandem, improvements are either needed in the performance of CdTe PVs with a substrate configuration (as opposed to superstrate), or superstrate CdTe PVs that exhibit high efficiency under reverse illumination. Neither one of these options are guaranteed to ever reach the high performance that is presently achieved in state-of-the-art commercial CdTe PVs.

It is also worth mentioning that although the 2T cells are preferred from an installation perspective (wiring, inverter integration, operation, etc), 4T designs do provide some preferred performance characteristics. For example, 4T designs allow for a greater variation in top cell bandgap energy to still achieve high performance (Werner et al., 2018a). The 4T configuration allows for greater process and materials flexibility since the materials in the two absorber layers can be processed independently. They also have a higher theoretical PCE due to relaxed current matching restrictions (Rühle, 2017). Therefore, we focus on the design and performance of a 4T HOIP-CdTe tandem cell, which seems most realistically realizable in the short-to-medium term.

3.3. A wide bandgap HOIP PV: Device characteristics and optical properties

As a first step towards realizing a perovskite/CdTe tandem solar cell, we fabricated a single junction MAPBr PV using the device architecture shown in Fig. 1b. Fig. 2a shows the response of the device under simulated sunlight. Devices with an ITO top contact were made with 3.5% PCE reverse scans, and an open circuit voltage of 1.35 V. Note that the transparent top and bottom contacts of these devices—particularly the ITO layer—have not been optimized and work on higher efficiency semi-transparent wide band gap HOIP PVs is ongoing. This involves for example the optimization of the ITO sputter deposition and use of a MoO_x interlayer. The optical properties of the functioning, semi-transparent MAPBr PV were then measured so that the HOIP-CdTe tandem cell performance could be modeled using SCAPS.

In the 4T device, light is being absorbed by the top MAPBr device layer and contributing to the power output of the device. Ideally, all of the photons that are not absorbed and converted into electricity make it through the top cell and reach the bottom CdTe cell. The optical loss from top cell illumination was measured, as shown in Fig. 2a and 2b. There is a sharp drop in transmitted light at wavelengths less than 540 nm, which corresponds to the expected bandgap of MAPBr of 2.3 eV. At wavelengths above 540 nm, there is also a reduction in transmitted light of about 25%. After accounting for all of the light incident on an FTO/TiO_2/MAPBr thin film using an integrating sphere, the specular reflectance, specular transmittance, and diffuse reflectance of the thin film were determined and the contributions of reflection, parasitic absorption, and scattering processes to optical losses were estimated. Fig. 2c shows that parasitic absorption and reflection

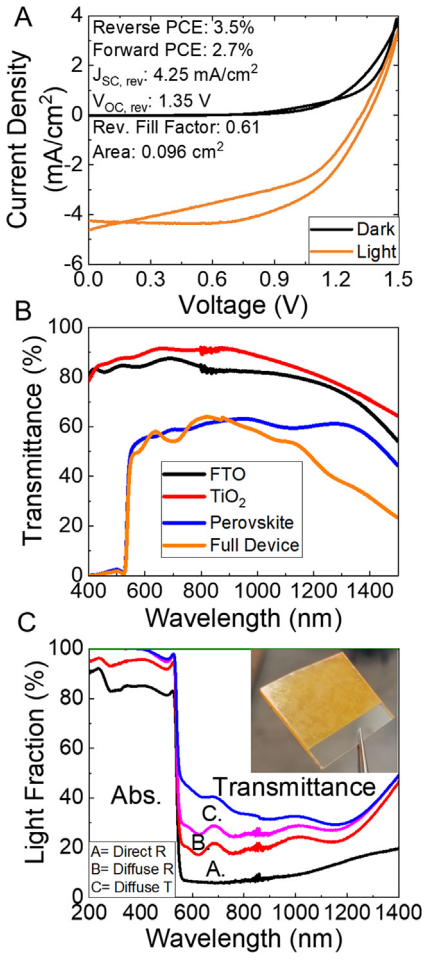

Fig. 2. (A) Current-voltage (*J-V*) curves for a semi-transparent $MAPbBr_3$ device. (B) Direct transmittance curves taken after each layer in the MAPBr device was deposited. Each label in the legend corresponds to the last layer of the device that was deposited, using an architecture similar to Fig. 1b, but with ITO instead of gold as a top contact (C) Full light accounting of all incident light on a MAPBr-coated TiO_2 substrate. We observe a large portion of optical loss in MAPBr films is due to diffuse reflectance and transmission (i.e. optical haze). The inset in (C) shows a photograph of the MAPBr-coated TiO_2 substrate.

accounts for about 20% of the optical loss in the sub-gap region, which agrees with previous reports (Guchhait et al., 2017; Jang et al., 2017; Rajagopal et al., 2017). However, diffuse light scattering, otherwise referred to as optical haze, also has a very large contribution to optical losses in the sub-gap region. Haze is defined formally as all transmitted light that is scattered more than 2.5° relative to the incident beam, or as all reflected light that is scattered more than 2.5° relative to the spot of specular reflection (ASTM International, 2015).

Differential image contrast (DIC) light microscopy of MAPBr deposited on TiO_2-coated FTO glass substrates revealed that the haze results from thickness non-uniformities in the perovskite layer. Fig. 3 shows DIC images and an SEM image of an MAPBr layer. DIC light microscopy is commonly used to characterize birefringent materials (Sigman and Korgel, 2005), but it also reveals spatial variations of light scattering (MacKintosh et al., 1989). Regions of the film with significant light scattering appear darker when imaged in parallel polarized orientation and brighter under crossed polarized orientation. The variations in light scattering in the film appear to correlate with surface roughness in the film, similar to the features referred to in the literature as “wrinkles” in $Cs_xFA_{1-x}Pb(Br_yI_{1-y})_3$ (Braunger et al., 2018; Bush et al., 2018) and $CsFAMAPbI_3$ (Bercegol et al., 2018). In one of these studies it

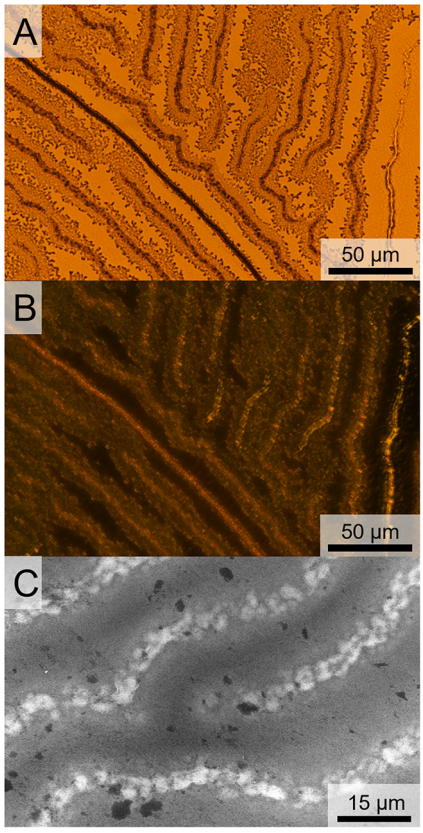

Fig. 3. DIC microscopy images of a MAPBr thin film with source and analyzer polarizers in a (A) parallel and (B) crossed/perpendicular orientation. (C) A top down SEM image of a MAPBr thin film. Film "wrinkling" is observed consistent with reports on lower band gap HOIPs (Braunger et al., 2018; Bush et al., 2018).

was mentioned that device layers made with wider band gap materials seem to always exhibit more wrinkles (Braunger et al., 2018). The DIC and SEM images indicate that it is the wrinkling of the MAPBr film that creates the observed haze. Perhaps alternative methods for depositing wide band gap HOIPs could alleviate this problem, such as two-step deposition processes (Yongfei Zhang et al., 2018), antisolvent engineering of the Hagfeldt process (Zheng et al., 2015), and the use of nanocrystals as opposed to bulk thin films (Hoffman et al., 2017). Ultimately, the optical quality of the films made using these processes must be considered alongside their performance in functioning solar cells in order to determine their viability in HOIP-CdTe tandems.

3.4. SCAPS modeling of 4T MAPBr-CdTe tandem devices

The device performance of 4T MAPBr/CdTe tandems was modeled using the measured optical and device characteristics of the MAPBr top cell and the Solar Cell Capacitance Simulator (SCAPS) software package using known parameters for CdTe devices (Burgelman et al., 2000; Kephart et al., 2015). Fig. 4 shows the *J-V* response of the CdTe bottom cell with a top cell having no haze or other sub-band gap optical loss. Device simulations of the CdTe cell were then performed considering the haze of the top cell by placing an appropriate optical filter over the CdTe bottom cell to mimic the 4T device. Less haze in the MAPBr layer is obviously desirable, but MAPBr device layers with higher PCE can tolerate more haze and still contribute to increasing the overall performance of a single junction CdTe PV. By subtracting the PCE of the filtered device from the PCE of the initial device, we determine the PCE of the top cell needed to "break even" or begin to improve

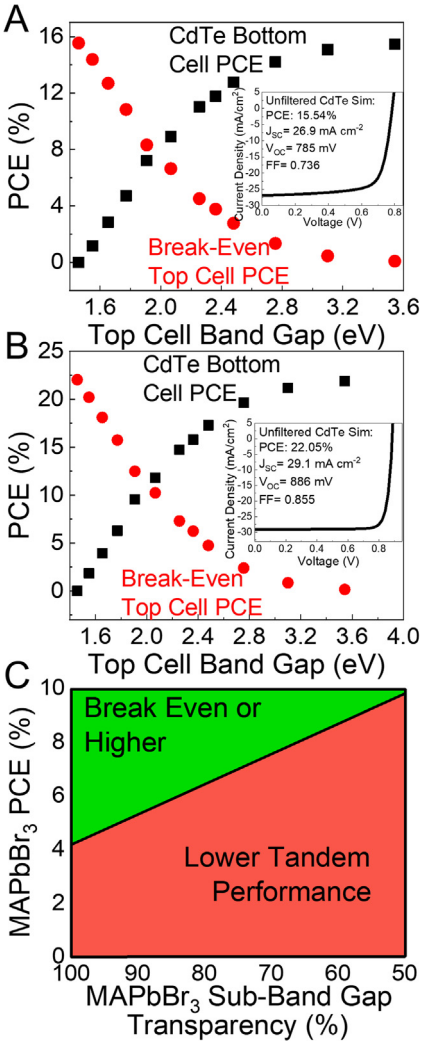

Fig. 4. Simulation of wide band gap semiconductor-CdTe tandem PVs, given a CdTe PCE of (A) 15.5% and (B) 22.05%. In both cases, we plot the "break even" top cell PCE, defined here as the PCE of the top cell that is needed for the tandem device to eclipse the PCE of the CdTe cell without the top cell acting as an optical filter. The insets show the simulated JV curves of the unfiltered CdTe device. (C) Break even PCE of a CdTe tandem cell as a function of the sub-band gap transmission of the top cell, given a 2.3 eV band gap top cell and 15.5% PCE CdTe device. With higher top cell optical losses, a higher top cell PCE is needed.

the efficiency of the system relative to the baseline single junction CdTe PV. The PCEs of the top perovskite cell needed to break even are shown in Fig. 4 for two different CdTe devices—the 15.5% PCE device of Kephart et al. (2015), and an optimized CdTe device with no defects and 22.05% PCE. For a MAPBr top cell (E_g = 2.3 eV) with 100% sub-band gap transmission and a 15.54% PCE CdTe bottom cell, an efficiency of at least 4.2% is needed to create a more efficient tandem. Note that the record PCE for MAPBr is 10.4% (Heo et al., 2014) and the Shockley-Queisser limit is 16.4% (Rühle, 2016). Using the commonly studied perovskite, $FA_{0.83}Cs_{0.17}Pb(I_{0.6}Br_{0.4})_3$ (E_g = 1.75 eV), at least 11.1% PCE is needed to break even. For reference, the literature record for $FA_{0.83}Cs_{0.17}Pb(I_{0.6}Br_{0.4})_3$ is 17.8% (Kim et al., 2018b), and the Shockley Queisser limit is 27.5% (Rühle, 2016). The efficiency needed to improve the efficiency of a 22.05% PCE CdTe device is higher, with break-even PCEs for MAPBr and $FA_{0.83}Cs_{0.17}Pb(I_{0.6}Br_{0.4})_3$ of 6.9% and 16.2%, respectively.

Tandems with MAPBr (E_g = 2.3 eV) top cells with haze were also simulated using SCAPS. For the simulations, top cell optical

transmission curves were simplified to have uniform optical loss across the sub-band gap region (constant transmission $E(h\nu) < E_{g,HOIP}$, 0% transmission $E(h\nu) > E_{g,HOIP}$). Fig. 4c shows the break-even curves simulated using SCAPS, for 15.5% CdTe devices. With MAPBr top cells exhibiting 75% optical transmittance sub-band gap, 6.9% efficiency is needed in the top cell for the HOIP-CdTe tandem to outperform the CdTe bottom cell.

To compare perovskite-CdTe tandems with other perovskite-based tandems, SCAPS device modeling was carried out using CIGS, methylammonium lead iodide (MAPI) and amorphous Si as a bottom cell. Fig. 5 summarizes the results in terms of the acceptable amount of optical loss for MAPBr pairings with a CIGS (E_g = 1.1 eV; 17.4% PCE), methylammonium lead iodide/MAPI (E_g = 1.5 eV; 21.5% PCE), and amorphous silicon (E_g = 1.82 eV; 12.3% PCE). Unfiltered simulated *J-V* curves for these three PVs are provided as supporting information (Fig. S2), and the parameters used in the device modeling are provided in Supporting Information (Tables S1–S3). For a MAPBr with 75% sub-band gap transmittance, the break-even PCE is 7.4%, 10.7%, and 8.4% respectively for CIGS, MAPI, and a-Si cells modeled here. The slightly higher break-even PCEs for the MAPI and CIGS tandems results in part from the higher PCE of the bottom cells.

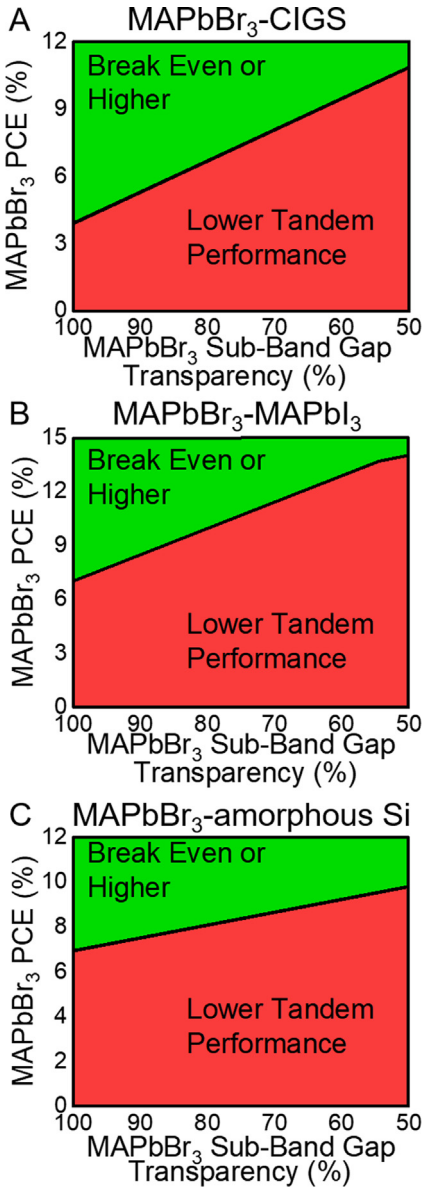

Fig. 5. Break even PCE of perovskite top cell tandems as a function of sub-band gap optical transmission with a 2.3 eV $CH_3NH_3PbBr_3$ top cell: (A) a 1.1 eV band gap CIGS cell with 17.4% PCE, (B) a 1.55 eV band gap $CH_3NH_3PbI_3$ PV with 21.5% PCE, and (C) a 1.82 eV band gap amorphous silicon PV with 12.3% PCE.

4. Conclusions

The approach of increasing CdTe PV efficiency by the addition of a wide bandgap perovskite layer in a 4T tandem device configuration appears to be a plausible way to increase efficiency without significantly increasing manufacturing cost. The 4T configuration leads to higher BOS costs than a 2T tandem, but the increased efficiency might make it worthwhile to pursue such a device configuration (Sofia et al., 2018). In addition to the need to fabricate 4T devices, another challenge to perovskite-CdTe tandem cells appears to be the occurrence of haze in perovskite layers with the wide band gap needed for efficient operation with CdTe. Haze deteriorates the performance of the tandem by preventing light from reaching the bottom cell. SCAPS device modeling shows that it should still be possible to improve upon the bottom CdTe cell efficiency with a top perovskite cell with some amount of haze, but the necessary efficiency for this becomes much higher when the CdTe cell efficiency further increases towards its ideal high efficiency. It will require further layer optimization to eliminate the "wrinkles" that cause haze. Another challenge will be in the fabrication of highly transparent, conductive top and bottom contacts for the MAPBr top cell to eliminate parasitic light absorption. Again, a 2T device configuration can help alleviate this problem; however, only if high efficiency can somehow be achieved from CdTe PVs with alternative device fabrication (i.e., substrate) or illumination conditions (i.e., reverse illumination). Since the point is to take advantage of the tremendous progress in developing low-cost high-throughput manufacturing of CdTe thin film PVs to make low-cost, higher efficiency tandems, it may be the best strategy to figure out device designs that do not require significant changes to the CdTe cell design and operation. This will probably be the main challenge facing the development of perovskite-CdTe tandem PV technology.

Conflict of interest

The authors declared that there is no conflict of interest.

Acknowledgment

The authors acknowledge financial support of this work from the Robert A. Welch Foundation (F-1464) and the NSF Industry/University Cooperative Research Center on Next Generation Photovoltaics (IIP-1540028, IIP-1822206, IIP-1540007, IIP-1821526). TDS acknowledges support by the United States Government under DoD, Air Force Office of Scientific Research, National Defense Science and Engineering Graduate (NDSEG) Fellowship, 32 CFR 168a. We would like to acknowledge Anna Webb for providing technical support for the DIC optical microscope.

Contributions

TDS and BAK synthesized and characterized perovskite thin films and PVs and performed SCAPS calculations. TMS and WSS designed the prospective tandem cell and assisted with SCAPS calculations.

Appendix A. Supplementary material

Supplementary data to this article can be found online at https://doi.org/10.1016/j.ces.2019.01.003.

References

Adhyaksa, G.W.P., Johlin, E., Garnett, E.C., 2017. Nanoscale back contact perovskite solar cell design for improved tandem efficiency. Nano Lett. 17, 5206–5212. https://doi.org/10.1021/acs.nanolett.7b01092.

Alberti, A., Deretzis, I., Mannino, G., Smecca, E., Sanzaro, S., Numata, Y., Miyasaka, T., La Magna, A., 2017. Revealing a discontinuity in the degradation behavior of $CH_3NH_3PbI_3$ during thermal operation. J. Phys. Chem. C 121, 13577–13585. https://doi.org/10.1021/acs.jpcc.7b04196.

Albrecht, S., Saliba, M., Correa Baena, J.P., Lang, F., Kegelmann, L., Mews, M., Steier, L., Abate, A., Rappich, J., Korte, L., Schlatmann, R., Nazeeruddin, M.K., Hagfeldt, A., Grätzel, M., Rech, B., 2016a. Monolithic perovskite/silicon-heterojunction tandem solar cells processed at low temperature. Energy Environ. Sci. 9, 81–88. https://doi.org/10.1039/C5EE02965A.

Albrecht, S., Saliba, M., Correa-Baena, J.P., Jäger, K., Korte, L., Hagfeldt, A., Grätzel, M., Rech, B., 2016b. Towards optical optimization of planar monolithic perovskite/silicon-heterojunction tandem solar cells. J. Opt. 18, 064012. https://doi.org/10.1088/2040-8978/18/6/064012.

Alsema, E.A., de Wild-Scholten, M.J., 2006. Environmental impacts of PV electricity generation – a critical comparison of energy supply options. In: Presented at the 21st European P.

ASTM International, 2015. Standard Test Method for Reflection Haze of High-Gloss Surfaces. ASTM International.

Ba, L., Liu, H., Shen, W., 2018. Perovskite/c-Si tandem solar cells with realistic inverted architecture: achieving high efficiency by optical optimization. Prog. Photovolt. Res. Appl. https://doi.org/10.1002/pip.3037.

Bailie, C.D., Christoforo, M.G., Mailoa, J.P., Bowring, A.R., Unger, E.L., Nguyen, W.H., Burschka, J., Pellet, N., Lee, J.Z., Grätzel, M., Noufi, R., Buonassisi, T., Salleo, A., McGehee, M.D., 2015. Semi-transparent perovskite solar cells for tandems with silicon and CIGS. Energy Environ. Sci. 8, 956–963. https://doi.org/10.1039/C4EE03322A.

Bercegol, A., Ramos, F.J., Rebai, A., Guillemot, T., Puel, J.-B., Guillemoles, J.-F., Ory, D., Rousset, J., Lombez, L., 2018. Spatial Inhomogeneity Analysis of Cesium-Rich Wrinkles in Triple-Cation Perovskites. J. Phys. Chem. C 122, 23345–23351 https://doi.org/10.1021/acs.jpcc.8b07436.

Bett, A.J., Schulze, P.S.C., Winkler, K., Gasparetto, J., Ndione, P.F., Bivour, M., Hinsch, A., Kohlstädt, M., Lee, S., Mastroianni, S., Mundt, L.E., Mundus, M., Reichel, C., Richter, A., Veit, C., Wienands, K., Würfel, U., Veurman, W., Glunz, S.W., Hermle, M., Goldschmidt, J.C., 2017. Low temperature perovskite solar cells with an evaporated TiO_2 compact layer for perovskite silicon tandem solar cells. Energy Procedia 124, 567–576. https://doi.org/10.1016/j.egypro.2017.09.293.

Braunger, S., Mundt, L.E., Wolff, C.M., Mews, M., Rehermann, C., Jošt, M., Tejada, A., Eisenhauer, D., Becker, C., Guerra, J.A., Unger, E., Korte, L., Neher, D., Schubert, M. C., Rech, B., Albrecht, S., 2018. $Cs_xFA_{1-x}Pb(I_{1-y}Br_y)_3$ perovskite compositions: the appearance of wrinkled morphology and its impact on solar cell performance. J. Phys. Chem. C 122, 17123–17135. https://doi.org/10.1021/acs.jpcc.8b06459.

Brown, G.F., Wu, J., 2009. Third generation photovoltaics. Laser Photon. Rev. 3, 394–405. https://doi.org/10.1002/lpor.200810039.

Burgelman, M., Nollet, P., Degrave, S., 2000. Modelling polycrystalline semiconductor solar cells. Thin Solid Films 361–362, 527–532. https://doi.org/10.1016/S0040-6090(99)00825-1.

Bush, K.A., Bailie, C.D., Chen, Y., Bowring, A.R., Wang, W., Ma, W., Leijtens, T., Moghadam, F., McGehee, M.D., 2016. Thermal and environmental stability of semi-transparent perovskite solar cells for tandems enabled by a solution-processed nanoparticle buffer layer and sputtered ITO electrode. Adv. Mater. 28, 3937–3943. https://doi.org/10.1002/adma.201505279.

Bush, K.A., Palmstrom, A.F., Yu, Z.J., Boccard, M., Cheacharoen, R., Mailoa, J.P., McMeekin, D.P., Hoye, R.L.Z., Bailie, C.D., Leijtens, T., Peters, I.M., Minichetti, M. C., Rolston, N., Prasanna, R., Sofia, S., Harwood, D., Ma, W., Moghadam, F., Snaith, H.J., Buonassisi, T., Holman, Z.C., Bent, S.F., McGehee, M.D., 2017. 23.6%-efficient monolithic perovskite/silicon tandem solar cells with improved stability. Nat. Energy 2, 17009. https://doi.org/10.1038/nenergy.2017.9.

Bush, K.A., Rolston, N., Gold-Parker, A., Manzoor, S., Hausele, J., Yu, Z.J., Raiford, J.A., Cheacharoen, R., Holman, Z.C., Toney, M.F., Dauskardt, R.H., McGehee, M.D., 2018. Controlling thin-film stress and wrinkling during perovskite film formation. ACS Energy Lett. 3, 1225–1232. https://doi.org/10.1021/acsenergylett.8b00544.

Chelvanathan, P., Hossain, M.I., Amin, N., 2010. Performance analysis of copper–indium–gallium–diselenide (CIGS) solar cells with various buffer layers by SCAPS. Curr. Appl. Phys. 10, S387–S391. https://doi.org/10.1016/j.cap.2010.02.018.

Chen, B., Bai, Y., Yu, Z., Li, T., Zheng, X., Dong, Q., Shen, L., Boccard, M., Gruverman, A., Holman, Z., Huang, J., 2016. Efficient semitransparent perovskite solar cells for 23.0%-efficiency perovskite/silicon four-terminal tandem cells. Adv. Energy Mater. 6, 1601128. https://doi.org/10.1002/aenm.201601128.

Chen, C.-C., Bae, S.-H., Chang, W.-H., Hong, Z., Li, G., Chen, Q., Zhou, H., Yang, Y., 2015. Perovskite/polymer monolithic hybrid tandem solar cells utilizing a low-temperature, full solution process. Mater. Horiz. 2, 203–211. https://doi.org/10.1039/C4MH00237G.

Chen, W., Zhang, J., Xu, G., Xue, R., Li, Y., Zhou, Y., Hou, J., Li, Y., 2018. A semitransparent inorganic perovskite film for overcoming ultraviolet light instability of organic solar cells and achieving 14.03% efficiency. Adv. Mater. 30, 1800855. https://doi.org/10.1002/adma.201800855.

Christians, J.A., Miranda Herrera, P.A., Kamat, P.V., 2015. Transformation of the excited state and photovoltaic efficiency of $CH_3NH_3PbI_3$ perovskite upon controlled exposure to humidified air. J. Am. Chem. Soc. 137, 1530–1538. https://doi.org/10.1021/ja511132a.

Compaan, A.D., Gupta, A., Lee, S., Wang, S., Drayton, J., 2004. High efficiency, magnetron sputtered CdS/CdTe solar cells. Sol. Energy 77, 815–822. https://doi.org/10.1016/j.solener.2004.06.013.

Dimroth, Frank, 2006. High-efficiency solar cells from III-V compound semiconductors. Phys. Stat. Sol. C, 3, 373–379. https://doi.org/10.1002/pssc.200564172.

Domanski, K., Correa-Baena, J.P., Mine, N., Nazeeruddin, M.K., Abate, A., Saliba, M., Tress, W., Hagfeldt, A., Grätzel, M., 2016. Not all that glitters is gold: metal-migration-induced degradation in perovskite solar cells. ACS Nano 10, 6306–6314. https://doi.org/10.1021/acsnano.6b02613.

Duong, T., Lal, N., Grant, D., Jacobs, D., Zheng, P., Rahman, S., Shen, H., Stocks, M., Blakers, A., Weber, K., White, T.P., Catchpole, K.R., 2016. Semitransparent perovskite solar cell with sputtered front and rear electrodes for a four-terminal tandem. IEEE J. Photovolt. 6, 679–687. https://doi.org/10.1109/JPHOTOV.2016.2521479.

Duong, T., Wu, Y., Shen, H., Peng, J., Fu, X., Jacobs, D., Wang, E.-C., Kho, T.C., Fong, K. C., Stocks, M., Franklin, E., Blakers, A., Zin, N., McIntosh, K., Li, W., Cheng, Y.-B., White, T.P., Weber, K., Catchpole, K., 2017. Rubidium multication perovskite with optimized bandgap for perovskite-silicon tandem with over 26% efficiency. Adv. Energy Mater. 7, 1700228. https://doi.org/10.1002/aenm.201700228.

Durose, K., Edwards, P.R., Halliday, D.P., 1999. Materials aspects of CdTe/CdS solar cells. J. Cryst. Growth 197, 733–742. https://doi.org/10.1016/S0022-0248(98)00962-2.

Eperon, G.E., Leijtens, T., Bush, K.A., Prasanna, R., Green, T., Wang, J.T.-W., McMeekin, D.P., Volonakis, G., Milot, R.L., May, R., Palmstrom, A., Slotcavage, D.J., Belisle, R. A., Patel, J.B., Parrott, E.S., Sutton, R.J., Ma, W., Moghadam, F., Conings, B., Babayigit, A., Boyen, H.-G., Bent, S., Giustino, F., Herz, L.M., Johnston, M.B., McGehee, M.D., Snaith, H.J., 2016. Perovskite-perovskite tandem photovoltaics with optimized band gaps. Science 354, 861–865. https://doi.org/10.1126/science.aaf9717.

Eperon, G.E., Paternò, G.M., Sutton, R.J., Zampetti, A., Haghighirad, A.A., Cacialli, F., Snaith, H.J., 2015. Inorganic caesium lead iodide perovskite solar cells. J. Mater. Chem. A 3, 19688–19695. https://doi.org/10.1039/C5TA06398A.

Fan, R., Zhou, N., Zhang, L., Yang, R., Meng, Y., Li, L., Guo, T., Chen, Y., Xu, Z., Zheng, G., Huang, Y., Li, Liang, Qin, L., Qiu, X., Chen, Q., Zhou, H., 2017. Toward full solution processed perovskite/si monolithic tandem solar device with PCE exceeding 20%. Sol. RRL 1, 1700149. https://doi.org/10.1002/solr.201700149.

Forgács, D., Gil-Escrig, L., Pérez-Del-Rey, D., Momblona, C., Werner, J., Niesen, B., Ballif, C., Sessolo, M., Bolink, H.J., 2017. Efficient monolithic perovskite/perovskite tandem solar cells. Adv. Energy Mater. 7, 1602121. https://doi.org/10.1002/aenm.201602121.

Fu, F., Feurer, T., Jäger, T., Avancini, E., Bissig, B., Yoon, S., Buecheler, S., Tiwari, A.N., 2015. Low-temperature-processed efficient semi-transparent planar perovskite solar cells for bifacial and tandem applications. Nat. Commun. 6. https://doi.org/10.1038/ncomms9932.

Fu, F., Feurer, T., Weiss, T.P., Pisoni, S., Avancini, E., Andres, C., Buecheler, S., Tiwari, A.N., 2016. High-efficiency inverted semi-transparent planar perovskite solar cells in substrate configuration. Nat. Energy 2, 16190. https://doi.org/10.1038/nenergy.2016.190.

Green, M.A., Hishikawa, Y., Dunlop, E.D., Levi, D.H., Hohl-Ebinger, J., Ho-Baillie, A.W. Y., 2018. Solar cell efficiency tables (version 52). Prog. Photovolt. Res. Appl. 26, 427–436. https://doi.org/10.1002/pip.3040.

Green, M.A., Ho-Baillie, A., Snaith, H.J., 2014. The emergence of perovskite solar cells. Nat. Photon. 8, 506–514. https://doi.org/10.1038/nphoton.2014.134.

Guchhait, A., Dewi, H.A., Leow, S.W., Wang, H., Han, G., Suhaimi, F.B., Mhaisalkar, S., Wong, L.H., Mathews, N., 2017. Over 20% efficient CIGS–perovskite tandem solar cells. ACS Energy Lett. 2, 807–812. https://doi.org/10.1021/acsenergylett.7b00187.

Han, Q., Hsieh, Y.-T., Meng, L., Wu, J.-L., Sun, P., Yao, E.-P., Chang, S.-Y., Bae, S.-H., Kato, T., Bermudez, V., Yang, Y., 2018. High-performance perovskite/Cu(In, Ga)Se_2 monolithic tandem solar cells. Science 361, 904–908.

Henbest, Seb, Giannakopoulou, E., and Cuming, V., 2015. New Energy Outlook 2015. Bloomberg Finance L.P., London, England. https://data.bloomberglp.com/bnef/sites/4/2015/06/BNEF-NEO2015_Executive-summary.pdf.

Hanne Degans, 2017. IMEC reports record conversion efficiency of 23.9 percent on a 4 cm2 perovskite/silicon solar module.

Hao, F., Stoumpos, C.C., Cao, D.H., Chang, R.P.H., Kanatzidis, M.G., 2014a. Lead-free solid-state organic–inorganic halide perovskite solar cells. Nat. Photon. 8, 489–494. https://doi.org/10.1038/nphoton.2014.82.

Hao, F., Stoumpos, C.C., Chang, R.P.H., Kanatzidis, M.G., 2014b. Anomalous band gap behavior in mixed Sn and Pb perovskites enables broadening of absorption spectrum in solar cells. J. Am. Chem. Soc. 136, 8094–8099. https://doi.org/10.1021/ja5033259.

Heo, J.H., Im, S.H., 2016. $CH_3NH_3PbBr_3$-$CH_3NH_3PbI_3$ perovskite-perovskite tandem solar cells with exceeding 2.2 V open circuit voltage. Adv. Mater. 28, 5121–5125. https://doi.org/10.1002/adma.201501629.

Heo, J.H., Song, D.H., Im, S.H., 2014. Planar $CH_3NH_3PbBr_3$ hybrid solar cells with 10.4% power conversion efficiency, fabricated by controlled crystallization in the spin-coating process. Adv. Mater. 26, 8179–8183. https://doi.org/10.1002/adma.201403140.

Hoffman, J.B., Zaiats, G., Wappes, I., Kamat, P.V., 2017. $CsPbBr_3$ solar cells: controlled film growth through layer-by-layer quantum dot deposition. Chem. Mater. 29, 9767–9774. https://doi.org/10.1021/acs.chemmater.7b03751.

Hoke, E.T., Slotcavage, D.J., Dohner, E.R., Bowring, A.R., Karunadasa, H.I., McGehee, M.D., 2015. Reversible photo-induced trap formation in mixed-halide hybrid perovskites for photovoltaics. Chem. Sci. 6, 613–617. https://doi.org/10.1039/C4SC03141E.

Holmberg, V.C., Bogart, T.D., Chockla, A.M., Hessel, C.M., Korgel, B.A., 2012. Optical properties of silicon and germanium nanowire fabric. J. Phys. Chem. C 116, 22486–22491. https://doi.org/10.1021/jp308231w.

IEA, 2017. Tracking Clean Energy Progress: 2017. IEA, Paris, France. https://www.iea.org/etp/tracking2017/.

Jang, Y.H., Lee, J.M., Seo, J.W., Kim, I., Lee, D.-K., 2017. Monolithic tandem solar cells comprising electrodeposited $CuInSe_2$ and perovskite solar cells with a nanoparticulate ZnO buffer layer. J. Mater. Chem. A 5, 19439–19446. https://doi.org/10.1039/C7TA06163C.

Jaysankar, M., Filipič, M., Zielinski, B., Schmager, R., Song, W., Qiu, W., Paetzold, U. W., Aernouts, T., Debucquoy, M., Gehlhaar, R., Poortmans, J., 2018. Perovskite–silicon tandem solar modules with optimised light harvesting. Energy Environ. Sci. 11, 1489–1498. https://doi.org/10.1039/C8EE00237A.

Jaysankar, M., Qiu, W., van Eerden, M., Aernouts, T., Gehlhaar, R., Debucquoy, M., Paetzold, U.W., Poortmans, J., 2017. Four-terminal perovskite/silicon multijunction solar modules. Adv. Energy Mater. 7, 1602807. https://doi.org/10.1002/aenm.201602807.

Jesper Jacobsson, T., Correa-Baena, J.-P., Pazoki, M., Saliba, M., Schenk, K., Grätzel, M., Hagfeldt, A., 2016. Exploration of the compositional space for mixed lead halogen perovskites for high efficiency solar cells. Energy Environ. Sci. 9, 1706–1724. https://doi.org/10.1039/C6EE00030D.

Jiang, F., Liu, T., Luo, B., Tong, J., Qin, F., Xiong, S., Li, Z., Zhou, Y., 2016. A two-terminal perovskite/perovskite tandem solar cell. J. Mater. Chem. A 4, 1208–1213. https://doi.org/10.1039/C5TA08744A.

Jošt, M., Albrecht, S., Lipovšek, B., Krč, J., Korte, L., Rech, B., Topič, M., 2016. Back- and front-side texturing for light-management in perovskite/silicon-heterojunction tandem solar cells. Energy Procedia 102, 43–48. https://doi.org/10.1016/j.egypro.2016.11.316.

Kapil, G., Ripolles, T.S., Hamada, K., Ogomi, Y., Bessho, T., Kinoshita, T., Chantana, J., Yoshino, K., Shen, Q., Toyoda, T., Minemoto, T., Murakami, T.N., Segawa, H., Hayase, S., 2018. Highly efficient 17.6% tin-lead mixed perovskite solar cells realized through spike structure. Nano Lett. 18, 3600–3607. https://doi.org/10.1021/acs.nanolett.8b00701.

Karani, A., Yang, L., Bai, S., Futscher, M.H., Snaith, H.J., Ehrler, B., Greenham, N.C., Di, D., 2018. Perovskite/colloidal quantum dot tandem solar cells: theoretical modeling and monolithic structure. ACS Energy Lett. 3, 869–874. https://doi.org/10.1021/acsenergylett.8b00207.

Kephart, J.M., Geisthardt, R.M., Sampath, W.S., 2015. Optimization of CdTe thin-film solar cell efficiency using a sputtered, oxygenated CdS window layer. Prog. Photovolt. Res. Appl. 23, 1484–1492. https://doi.org/10.1002/pip.2578.

Kephart, J.M., McCamy, J.W., Ma, Z., Ganjoo, A., Alamgir, F.M., Sampath, W.S., 2016. Band alignment of front contact layers for high-efficiency CdTe solar cells. Solar Energy Materials and Solar Cells 157, 266–275.

Kim, J., Ouellette, O., Voznyy, O., Wei, M., Choi, J., Choi, M.-J., Jo, J.W., Baek, S.-W., Fan, J., Saidaminov, M.I., Sun, B., Li, P., Nam, D.-H., Hoogland, S., Lu, Z.-H., García de Arquer, F.P., Sargent, E.H., 2018a. Butylamine-catalyzed synthesis of nanocrystal inks enables efficient infrared CQD solar cells. Adv. Mater. 30, 1803830. https://doi.org/10.1002/adma.201803830.

Kim, J., Saidaminov, M.I., Tan, H., Zhao, Y., Kim, Y., Choi, J., Jo, J.W., Fan, J., Quintero-Bermudez, R., Yang, Z., Quan, L.N., Wei, M., Voznyy, O., Sargent, E.H., 2018b. Amide-catalyzed phase-selective crystallization reduces defect density in wide-bandgap perovskites. Adv. Mater. 30, 1706275. https://doi.org/10.1002/adma.201706275.

Kinoshita, T., Nonomura, K., Joong Jeon, N., Giordano, F., Abate, A., Uchida, S., Kubo, T., Seok, S.I., Nazeeruddin, M.K., Hagfeldt, A., Grätzel, M., Segawa, H., 2015. Spectral splitting photovoltaics using perovskite and wideband dye-sensitized solar cells. Nat. Commun. 6, 8834. https://doi.org/10.1038/ncomms9834.

Kranz, L., Abate, A., Feurer, T., Fu, F., Avancini, E., Löckinger, J., Reinhard, P., Zakeeruddin, S.M., Grätzel, M., Buecheler, S., Tiwari, A.N., 2015. High-efficiency polycrystalline thin film tandem solar cells. J. Phys. Chem. Lett. 6, 2676–2681. https://doi.org/10.1021/acs.jpclett.5b01108.

Kranz, L., Schmitt, R., Gretener, C., Perrenoud, J., Pianezzi, F., Uhl, A.R., Keller, D., Buecheler, S., Tiwari, A.N., 2013. Progress towards 14% efficient CdTe solar cells in substrate configuration. In: IEEE Photovoltaics Specialists Conference (PVSC), pp. 1644–1648 https://doi.org/10.1109/PVSC.2013.6744460.

Kulbak, M., Gupta, S., Kedem, N., Levine, I., Bendikov, T., Hodes, G., Cahen, D., 2016. Cesium enhances long-term stability of lead bromide perovskite-based solar cells. J. Phys. Chem. Lett. 7, 167–172. https://doi.org/10.1021/acs.jpclett.5b02597.

Lal, N.N., Dkhissi, Y., Li, W., Hou, Q., Cheng, Y.-B., Bach, U., 2017. Perovskite tandem solar cells. Adv. Energy Mater. 7, 1602761. https://doi.org/10.1002/aenm.201602761.

Lazard Inc., 2018. Lazard's Levelized Cost of Energy, Version 11.0. Lazard, New York, NY, USA. https://www.lazard.com/media/450784/lazards-levelized-cost-of-energy-version-120-vfinal.pdf

Lee, C., Efstathiadis, H., Raynolds, J.E., Haldar, P., 2009. Two-dimensional computer modeling of single junction a-Si: H solar cells. In: IEEE Photovoltaic Specialists Conference (PVSC), pp. 1118–1122 https://doi.org/10.1109/PVSC.2009.5411215.

Lee, J.-W., Seol, D.-J., Cho, A.-N., Park, N.-G., 2014. High-efficiency perovskite solar cells based on the black polymorph of $HC(NH_2)_2PbI_3$. Adv. Mater. 26, 4991–4998. https://doi.org/10.1002/adma.201401137.

Leijtens, T., Prasanna, R., Bush, K.A., Eperon, G., Raiford, J.A., Gold-Parker, A., Wolf, E. J., Swifter, S.A., Boyd, C.C., Wang, H.-P., Toney, M.F., Bent, S., McGehee, M.D., 2018. Tin-lead halide perovskites with improved thermal and air stability for efficient all-perovskite tandem solar cells. Sustain. Energy Fuels 2, 2450–2459. https://doi.org/10.1039/C8SE00314A.

Li, Y., Hu, H., Chen, B., Salim, T., Zhang, J., Ding, J., Yuan, N., Lam, Y.M., 2017. Reflective perovskite solar cells for efficient tandem applications. J. Mater. Chem. C 5, 134–139. https://doi.org/10.1039/C6TC04510C.

Liu, M., Johnston, M.B., Snaith, H.J., 2013. Efficient planar heterojunction perovskite solar cells by vapour deposition. Nature 501, 395–398. https://doi.org/10.1038/nature12509.

Liu, Y., Renna, L.A., Bag, M., Page, Z.A., Kim, P., Choi, J., Emrick, T., Venkataraman, D., Russell, T.P., 2016. High efficiency tandem thin-perovskite/polymer solar cells with a graded recombination layer. ACS Appl. Mater. Interfaces 8, 7070–7076. https://doi.org/10.1021/acsami.5b12740.

Long, M., Zhang, T., Liu, M., Chen, Z., Wang, C., Xie, W., Xie, F., Chen, J., Li, G., Xu, J., 2018. Abnormal synergetic effect of organic and halide ions on the stability and optoelectronic properties of a mixed perovskite via in situ characterizations. Adv. Mater. 30, 1801562. https://doi.org/10.1002/adma.201801562.

Löper, P., Moon, S.-J., de Nicolas, S.M., Niesen, B., Ledinsky, M., Nicolay, S., Bailat, J., Yum, J.-H., De Wolf, S., Ballif, C., 2015. Organic–inorganic halide perovskite/crystalline silicon four-terminal tandem solar cells. Phys. Chem. Chem. Phys. 17, 1619–1629. https://doi.org/10.1039/C4CP03788J.

MacKintosh, F.C., Zhu, J.X., Pine, D.J., Weitz, D.A., 1989. Polarization memory of multiply scattered light. Phys. Rev. B 40, 9342–9345. https://doi.org/10.1103/PhysRevB.40.9342.

Mailoa, J.P., Bailie, C.D., Johlin, E.C., Hoke, E.T., Akey, A.J., Nguyen, W.H., McGehee, M. D., Buonassisi, T., 2015. A 2-terminal perovskite/silicon multijunction solar cell enabled by a silicon tunnel junction. Appl. Phys. Lett. 106, 121105. https://doi.org/10.1063/1.4914179.

Mailoa, J.P., Lee, M., Peters, I.M., Buonassisi, T., Panchula, A., Weiss, D.N., 2016. Energy-yield prediction for II–VI-based thin-film tandem solar cells. Energy Environ. Sci. 9, 2644–2653. https://doi.org/10.1039/C6EE01778A.

Mayer, J.N., Phillips, S., Hussein, N. S., Shlegl, T., and Senkpiel, C., 2015. Current and Future Cost of Photovoltaics. Fraunhofer ISE, Freiburg, Germany. https://www.ise.fraunhofer.de/content/dam/ise/de/documents/publications/studies/AgoraEnergiewende_Current_and_Future_Cost_of_PV_Feb2015_web.pdf

McMeekin, D.P., Sadoughi, G., Rehman, W., Eperon, G.E., Saliba, M., Hörantner, M.T., Haghighirad, A., Sakai, N., Korte, L., Rech, B., Johnston, M.B., Herz, L.M., Snaith, H. J., 2016. A mixed-cation lead mixed-halide perovskite absorber for tandem solar cells. Science 351, 151–155. https://doi.org/10.1126/science.aad5845.

Munshi, A. and Sampath, W.S., 2016. CdTe Photovoltaics for Sustainable Electricity Generation. Journal of Electronic Materials, 45, 4612–4619. http://doi.org/10.1007/s11664-016-4484-7.

Munshi, A.H., Kephart, J., Abbas, A., Raguse, J., Beaudry, J.-N., Barth, K., Sites, J., Walls, J., Sampath, W., 2018. Polycrystalline CdSeTe/CdTe absorber cells with 28 mA/cm^2 short-circuit current. IEEE J. Photovolt. 8, 310–314. https://doi.org/10.1109/JPHOTOV.2017.2775139.

Nelson, Jenny, 2003. The Physics of Solar Cells. Imperial College Press, London.

Noh, J.H., Im, S.H., Heo, J.H., Mandal, T.N., Seok, S.I., 2013. Chemical management for colorful, efficient, and stable inorganic-organic hybrid nanostructured solar cells. Nano Lett. 13, 1764–1769. https://doi.org/10.1021/nl400349b.

Paetzold, U.W., Jaysankar, M., Gehlhaar, R., Ahlswede, E., Paetel, S., Qiu, W., Bastos, J., Rakocevic, L., Richards, B.S., Aernouts, T., Powalla, M., Poortmans, J., 2017. Scalable perovskite/CIGS thin-film solar module with power conversion efficiency of 17.8%. J. Mater. Chem. A 5, 9897–9906. https://doi.org/10.1039/C7TA01651D.

Parrott, E.S., Green, T., Milot, R.L., Johnston, M.B., Snaith, H.J., Herz, L.M., 2018. Interplay of structural and optoelectronic properties in formamidinium mixed tin-lead triiodide perovskites. Adv. Funct. Mater. 28, 1802803. https://doi.org/10.1002/adfm.201802803.

Peng, J., Duong, T., Zhou, X., Shen, H., Wu, Y., Mulmudi, H.K., Wan, Y., Zhong, D., Li, J., Tsuzuki, T., Weber, K.J., Catchpole, K.R., White, T.P., 2017. Efficient indium-doped TiO_x electron transport layers for high-performance perovskite solar cells and perovskite-silicon tandems. Adv. Energy Mater. 7, 1601768. https://doi.org/10.1002/aenm.201601768.

Pisoni, S., Fu, F., Feurer, T., Makha, M., Bissig, B., Nishiwaki, S., Tiwari, A.N., Buecheler, S., 2017. Flexible NIR-transparent perovskite solar cells for all-thin-film tandem photovoltaic devices. J. Mater. Chem. A 5, 13639–13647. https://doi.org/10.1039/C7TA04225F.

Rajagopal, A., Yang, Z., Jo, S.B., Braly, I.L., Liang, P.-W., Hillhouse, H.W., Jen, A.K.-Y., 2017. Highly efficient perovskite-perovskite tandem solar cells reaching 80% of the theoretical limit in photovoltage. Adv. Mater. 29, 1702140. https://doi.org/10.1002/adma.201702140.

Ramírez Quiroz, C.O., Shen, Y., Salvador, M., Forberich, K., Schrenker, N., Spyropoulos, G.D., Heumüller, T., Wilkinson, B., Kirchartz, T., Spiecker, E., Verlinden, P.J., Zhang, X., Green, M.A., Ho-Baillie, A., Brabec, C.J., 2018. Balancing electrical and optical losses for efficient 4-terminal Si–perovskite solar cells with solution processed percolation electrodes. J. Mater. Chem. A 6, 3583–3592. https://doi.org/10.1039/C7TA10945H.

Raugei, M., Bargigli, S., Ulgiati, S., 2007. Life cycle assessment and energy pay-back time of advanced photovoltaic modules: CdTe and CIS compared to poly-Si. Energy 32, 1310–1318. https://doi.org/10.1016/j.energy.2006.10.003.

Rehman, W., McMeekin, D.P., Patel, J.B., Milot, R.L., Johnston, M.B., Snaith, H.J., Herz, L.M., 2017. Photovoltaic mixed-cation lead mixed-halide perovskites: links between crystallinity, photo-stability and electronic properties. Energy Environ. Sci. 10, 361–369. https://doi.org/10.1039/C6EE03014A.

Rehman, W., Milot, R.L., Eperon, G.E., Wehrenfennig, C., Boland, J.L., Snaith, H.J., Johnston, M.B., Herz, L.M., 2015. Charge-carrier dynamics and mobilities in formamidinium lead mixed-halide perovskites. Adv. Mater. 27, 7938–7944. https://doi.org/10.1002/adma.201502969.

Rühle, S., 2017. The detailed balance limit of perovskite/silicon and perovskite/CdTe tandem solar cells. Phys. Status Solidi A 214, 1600955. https://doi.org/10.1002/pssa.201600955.

Rühle, S., 2016. Tabulated values of the Shockley-Queisser limit for single junction solar cells. Sol. Energy 130, 139–147. https://doi.org/10.1016/j.solener.2016.02.015.

Sahli, F., Kamino, B.A., Werner, J., Bräuninger, M., Paviet-Salomon, B., Barraud, L., Monnard, R., Seif, J.P., Tomasi, A., Jeangros, Q., Hessler-Wyser, A., De Wolf, S., Despeisse, M., Nicolay, S., Niesen, B., Ballif, C., 2018a. Improved optics in monolithic perovskite/silicon tandem solar cells with a nanocrystalline silicon recombination junction. Adv. Energy Mater. 8, 1701609. https://doi.org/10.1002/aenm.201701609.

Sahli, F., Werner, J., Kamino, B.A., Bräuninger, M., Monnard, R., Paviet-Salomon, B., Barraud, L., Ding, L., Diaz Leon, J.J., Sacchetto, D., Cattaneo, G., Despeisse, M., Boccard, M., Nicolay, S., Jeangros, Q., Niesen, B., Ballif, C., 2018b. Fully textured monolithic perovskite/silicon tandem solar cells with 25.2% power conversion efficiency. Nat. Mater. https://doi.org/10.1038/s41563-018-0115-4.

Schneider, B.W., Lal, N.N., Baker-Finch, S., White, T.P., 2014. Pyramidal surface textures for light trapping and antireflection in perovskite-on-silicon tandem solar cells. Opt. Express 22, A1422–A1430. https://doi.org/10.1364/OE.22.0A1422.

SEIA and Greentech Media, 2017. Solar Market Insight Report 2016 Year in Review. SEIA, Washington, DC, USA. https://www.seia.org/research-resources/solar-market-insight-report-2016-year-review.

Shah, A., Torres, P., Tscharner, R., Wyrsch, N., Keppner, H., 1999. Photovoltaic Technology: The Case for Thin-Film Solar Cells. Science, 285, 692–698. http://doi.org/10.1126/science.285.5428.692.

Shen, H., Duong, T., Peng, J., Jacobs, D., Wu, N., Gong, J., Wu, Y., Karuturi, S.K., Fu, X., Weber, K., Xiao, X., White, T.P., Catchpole, K., 2018. Mechanically-stacked perovskite/CIGS tandem solar cells with efficiency of 23.9% and reduced oxygen sensitivity. Energy Environ. Sci. 11, 394–406. https://doi.org/10.1039/C7EE02627G.

Sheng, R., Ho-Baillie, A.W.Y., Huang, S., Keevers, M., Hao, X., Jiang, L., Cheng, Y.-B., Green, M.A., 2015. Four-terminal tandem solar cells using $CH_3NH_3PbBr_3$ by spectrum splitting. J. Phys. Chem. Lett. 6, 3931–3934. https://doi.org/10.1021/acs.jpclett.5b01608.

Sheng, R., Hörantner, M.T., Wang, Z., Jiang, Y., Zhang, W., Agosti, A., Huang, S., Hao, X., Ho-Baillie, A., Green, M., Snaith, H.J., 2017. Monolithic wide band gap perovskite/perovskite tandem solar cells with organic recombination layers. J. Phys. Chem. C 121, 27256–27262. https://doi.org/10.1021/acs.jpcc.7b05517.

Shi, D., Zeng, Y., Shen, W., 2015. Perovskite/c-Si tandem solar cell with inverted nanopyramids: realizing high efficiency by controllable light trapping. Sci. Rep. 5, 16504. https://doi.org/10.1038/srep16504.

Sigman, M.B., Korgel, B.A., 2005. Strongly birefringent $Pb_3O_2Cl_2$ nanobelts. J. Am. Chem. Soc. 127, 10089–10095. https://doi.org/10.1021/ja051956i.

Slavney, A.H., Leppert, L., Saldivar Valdes, A., Bartesaghi, D., Savenije, T.J., Neaton, J. B., Karunadasa, H., 2018. Small-bandgap halide double perovskites. Angew. Chem. Int. Ed. 57, 12765–12770. https://doi.org/10.1002/anie.201807421.

Sofia, S.E., Mailoa, J.P., Weiss, D.N., Stanbery, B.J., Buonassisi, T., Peters, I.M., 2018. Economic viability of thin-film tandem solar modules in the United States. Nat. Energy 3, 387–394. https://doi.org/10.1038/s41560-018-0126-z.

Song, Z., McElvany, C.L., Phillips, A.B., Celik, I., Krantz, P.W., Watthage, S.C., Liyanage, G.K., Apul, D., Heben, M.J., 2017. A technoeconomic analysis of perovskite solar module manufacturing with low-cost materials and techniques. Energy Environ. Sci. 10, 1297–1305. https://doi.org/10.1039/C7EE00757D.

Song, Z., Werner, J., Shrestha, N., Sahli, F., De Wolf, S., Niesen, B., Watthage, S.C., Phillips, A.B., Ballif, C., Ellingson, R.J., Heben, M.J., 2016. Probing photocurrent nonuniformities in the subcells of monolithic perovskite/silicon tandem solar cells. J. Phys. Chem. Lett. 7, 5114–5120. https://doi.org/10.1021/acs.jpclett.6b02415.

Sutton, R.J., Eperon, G.E., Miranda, L., Parrott, E.S., Kamino, B.A., Patel, J.B., Hörantner, M.T., Johnston, M.B., Haghighirad, A.A., Moore, D.T., Snaith, H.J., 2016. Bandgap-tunable cesium lead halide perovskites with high thermal stability for efficient solar cells. Adv. Energy Mater. 6, 1502458. https://doi.org/10.1002/aenm.201502458.

Swanson, D.E., Reich, C., Abbas, A., Shimpi, T., Liu, H., Ponce, F.A., Walls, J.M., Zhang, Y.-H., Metzger, W.K., Sampath, W.S., Holman, Z.C., 2018. $CdCl_2$ passivation of polycrystalline CdMgTe and CdZnTe absorbers for tandem photovoltaic cells. J. Appl. Phys. 123, 203101. https://doi.org/10.1063/1.5023811.

Todorov, T., Gershon, T., Gunawan, O., Lee, Y.S., Sturdevant, C., Chang, L.-Y., Guha, S., 2015. Monolithic perovskite-CIGS tandem solar cells via in situ band gap engineering. Adv. Energy Mater. 5, 1500799. https://doi.org/10.1002/aenm.201500799.

Todorov, T., Gershon, T., Gunawan, O., Sturdevant, C., Guha, S., 2014. Perovskite-kesterite monolithic tandem solar cells with high open-circuit voltage. Appl. Phys. Lett. 105, 173902. https://doi.org/10.1063/1.4899275.

Todorov, T.K., Gunawan, O., Guha, S., 2018. Halide Perovskite Tandem Solar Cells. In: Sum, T.C., Mathews, N. (Eds.), Halide Perovskites: Photovoltaics, Light Emitting Devices, and Beyond. Wiley-VCH Verlag GmbH & Co, KGaA, Weinheim, Germany.

Uhl, A.R., Yang, Z., Jen, A.K.-Y., Hillhouse, H.W., 2017. Solution-processed chalcopyrite–perovskite tandem solar cells in bandgap-matched two- and four-terminal architectures. J. Mater. Chem. A 5, 3214–3220. https://doi.org/10.1039/C7TA00562H.

Uzu, H., Ichikawa, M., Hino, M., Nakano, K., Meguro, T., Hernández, J.L., Kim, H.-S., Park, N.-G., Yamamoto, K., 2015. High efficiency solar cells combining a perovskite and a silicon heterojunction solar cells via an optical splitting system. Appl. Phys. Lett. 106, 013506. https://doi.org/10.1063/1.4905177.

Voggu, V.R., Sham, J., Pfeffer, S., Pate, J., Fillip, L., Harvey, T.B., Brown Jr., R.M., Korgel, B.A., 2017. Flexible $CuInSe_2$ nanocrystal solar cells on paper. ACS Energy Lett. 2, 574–581. https://doi.org/10.1021/acsenergylett.7b00001.

Vos, A.D., 1980. Detailed balance limit of the efficiency of tandem solar cells. J. Phys. D: Appl. Phys. 13, 839–846. https://doi.org/10.1088/0022-3727/13/5/018.

Wang, Y., Fu, W., Yan, J., Chen, J., Yang, W., Chen, H., 2018. Low-bandgap mixed tin–lead iodide perovskite with large grains for high performance solar cells. J. Mater. Chem. A 6, 13090–13095. https://doi.org/10.1039/C8TA03054E.

Werner, J., Barraud, L., Walter, A., Bräuninger, M., Sahli, F., Sacchetto, D., Tétreault, N., Paviet-Salomon, B., Moon, S.-J., Allebé, C., Despeisse, M., Nicolay, S., De Wolf, S., Niesen, B., Ballif, C., 2016a. Efficient near-infrared-transparent perovskite solar cells enabling direct comparison of 4-terminal and monolithic perovskite/silicon tandem cells. ACS Energy Lett. 1, 474–480. https://doi.org/10.1021/acsenergylett.6b00254.

Werner, J., Dubuis, G., Walter, A., Löper, P., Moon, S.-J., Nicolay, S., Morales-Masis, M., De Wolf, S., Niesen, B., Ballif, C., 2015. Sputtered rear electrode with broadband transparency for perovskite solar cells. Sol. Energy Mater. Sol. Cells 141, 407–413. https://doi.org/10.1016/j.solmat.2015.06.024.

Werner, J., Niesen, B., Ballif, C., 2018a. Perovskite/silicon tandem solar cells: marriage of convenience or true love story? – An overview. Adv. Mater. Interfaces 5, 1700731. https://doi.org/10.1002/admi.201700731.

Werner, J., Sahli, F., Fu, F., Diaz Leon, J.J., Walter, A., Kamino, B.A., Niesen, B., Nicolay, S., Jeangros, Q., Ballif, C., 2018b. Perovskite/perovskite/silicon monolithic triple-junction solar cells with a fully textured design. ACS Energy Lett. 3, 2052–2058. https://doi.org/10.1021/acsenergylett.8b01165.

Werner, J., Walter, A., Rucavado, E., Moon, S.-J., Sacchetto, D., Rienaecker, M., Peibst, R., Brendel, R., Niquille, X., De Wolf, S., Löper, P., Morales-Masis, M., Nicolay, S., Niesen, B., Ballif, C., 2016b. Zinc tin oxide as high-temperature stable recombination layer for mesoscopic perovskite/silicon monolithic tandem solar cells. Appl. Phys. Lett. 109, 233902. https://doi.org/10.1063/1.4971361.

Werner, J., Weng, C.-H., Walter, A., Fesquet, L., Seif, J.P., De Wolf, S., Niesen, B., Ballif, C., 2016c. Efficient monolithic perovskite/silicon tandem solar cell with cell area >1 cm^2. J. Phys. Chem. Lett. 7, 161–166. https://doi.org/10.1021/acs.jpclett.5b02686.

Wu, Y., Yan, D., Peng, J., Duong, T., Wan, Y., Phang, S.P., Shen, H., Wu, N., Barugkin, C., Fu, X., Surve, S., Grant, D., Walter, D., White, T.P., Catchpole, K.R., Weber, K.J., 2017. Monolithic perovskite/silicon-homojunction tandem solar cell with over 22% efficiency. Energy Environ. Sci. 10, 2472–2479. https://doi.org/10.1039/C7EE02288C.

Yang, Y. (Michael), Chen, Q., Hsieh, Y.-T., Song, T.-B., Marco, N.D., Zhou, H., Yang, Y., 2015. Multilayer transparent top electrode for solution processed perovskite/Cu (In, Ga)(Se, S)$_2$ four terminal tandem solar cells. ACS Nano 9, 7714–7721. https://doi.org/10.1021/acsnano.5b03189.

Yang, Z., Rajagopal, A., Chueh, C.-C., Jo, S.B., Liu, B., Zhao, T., Jen, A.K.-Y., 2016. Stable low-bandgap Pb-Sn binary perovskites for tandem solar cells. Adv. Mater. 28, 8990–8997. https://doi.org/10.1002/adma.201602696.

Zhang, Yongfei, Liang, Y., Wang, Y., Guo, F., Sun, L., Xu, D., 2018a. Planar $FAPbBr_3$ solar cells with power conversion efficiency above 10%. ACS Energy Lett. 3, 1808–1814. https://doi.org/10.1021/acsenergylett.8b00540.

Zhang, Yaokang, Wu, Z., Li, P., Ono, L.K., Qi, Y., Zhou, J., Shen, H., Surya, C., Zheng, Z., 2018b. Fully solution-processed TCO-free semitransparent perovskite solar cells for tandem and flexible applications. Adv. Energy Mater. 8, 1701569. https://doi.org/10.1002/aenm.201701569.

Zhao, D., Wang, C., Song, Z., Yu, Y., Chen, C., Zhao, X., Zhu, K., Yan, Y., 2018. Four-terminal all-perovskite tandem solar cells achieving power conversion efficiencies exceeding 23%. ACS Energy Lett. 3, 305–306. https://doi.org/10.1021/acsenergylett.7b01287.

Zhao, D., Yu, Y., Wang, C., Liao, W., Shrestha, N., Grice, C.R., Cimaroli, A.J., Guan, L., Ellingson, R.J., Zhu, K., Zhao, X., Xiong, R.-G., Yan, Y., 2017. Low-bandgap mixed tin–lead iodide perovskite absorbers with long carrier lifetimes for all-perovskite tandem solar cells. Nat. Energy 2, 17018. https://doi.org/10.1038/nenergy.2017.18.

Zheng, J., Lau, C.F.J., Mehrvarz, H., Ma, F.-J., Jiang, Y., Deng, X., Soeriyadi, A., Kim, J., Zhang, M., Hu, L., Cui, X., Lee, D.S., Bing, J., Cho, Y., Chen, C., Green, M.A., Huang, S., Ho-Baillie, A.W.Y., 2018. Large area efficient interface layer free monolithic perovskite/homo-junction-silicon tandem solar cell with over 20% efficiency. Energy Environ. Sci. 11, 2432–2443. https://doi.org/10.1039/C8EE00689J.

Zheng, X., Chen, B., Wu, C., Priya, S., 2015. Room temperature fabrication of CH_3NH_3PbBr 3 by anti-solvent assisted crystallization approach for perovskite solar cells with fast response and small *J*-V hysteresis. Nano Energy 17, 269–278. https://doi.org/10.1016/j.nanoen.2015.08.023.